



Amorphous Ta₂O_xN_y-enwrapped TiO₂ rutile nanorods for enhanced solar photoelectrochemical water splitting

Hongwen Zhang^{a,1}, Lei Ma^{b,1}, Jintao Ming^a, Bingqian Liu^a, Yibo Zhao^a, Yidong Hou^a, Zhengxin Ding^a, Chao Xu^a, Zizhong Zhang^a, Jinlin Long^{a,*}

^a State Key Lab of Photocatalysis on Energy and Environment, College of Chemistry, Fuzhou University, Fuzhou, 350116, PR China

^b School of New Materials and New Energies, Shenzhen Technology University, Shenzhen, 518118, PR China

ARTICLE INFO

Keywords:

Photoelectrocatalysis
Water splitting
Photoanode
TiO₂ nanorods
Ta₂O_xN_y
Core-shell nanostructures

ABSTRACT

This work demonstrated the 12 fold-enhanced solar water splitting over the type-II core-shell nanostructured TiO₂ rutile photoanodes by orienting the charge flow and accelerating the hole transport to water-oxidation sites. Such nanoheterostructured photoanodes were designed rationally and prepared by a facile strategy to enwrapping an amorphous Ta₂O_xN_y layer on surface of TiO₂ nanorods grown on the FTO glass substrates, consequently the incident photon-to-current conversion efficiency was increased from 2.2% to 22.6% in a two-electrode system under 390 nm light irradiation. The activity results showed that under AM 1.5 G illumination, the photocurrent output of TiO₂@Ta₂O_xN_y photoanodes reached a stable density of 1.32 mA cm⁻² at 1.23 V vs RHE, and which is 12 times and ca. 4.3 times than that of the pristine TiO₂ and TiO₂@Ta₂O₅ counterparts, respectively. Correspondingly, the oxygen evolution rate was improved from 20.3 to 112.7 mmol m⁻² h⁻¹. A solar-to-chemical energy conversion efficiency of ca. 1.49% was achieved at 1.23 V vs RHE.

1. Introduction

Converting solar energy into hydrogen energy by photoelectrocatalytic (PEC) or photocatalytic (PC) water-splitting is one promising approach to quest for more efficient, clean and cheap energy sources. A large amount of work was focused on development of novel, efficient photoelectrodes and suspended photocatalysts that can work for the overall water splitting to H₂ and O₂ under visible light, even near infrared (NIR) light irradiation [1–8]. State-of-the-art PEC and PC systems for the conversion has been promoted to an efficiency as high as 4.7% using a triple junction amorphous silicon cell, but easily subject from photocorrosion [9,10]. In numerous photoelectrode materials reported over the past 10–20 years, metal oxide materials with suitable properties (chemical stability, high carrier mobilities and long carrier lifetimes) are more amenable to cheap, large-scale applications of PEC water splitting [11–15].

Among these metal oxides, rutile TiO₂ with a bandgap energy of ca. 3.0 eV is one of the crucial and extensively-explored materials applied in the PEC and PC water splitting due to its facile synthesis, natural abundance, low cost, and low toxicity to environment [16–19]. However, two intrinsic drawbacks shade largely its application vista of the

semiconductor photocatalyst. The first one is the large binding energy of excitons up to 130 meV, which lowers severally charge mobility and separation in bulk of rutile TiO₂ [20]. The second one is the narrow optical absorption cutoff a small fraction of incident solar photons (less than 5% UV), which leads to a low light-harvesting efficiency [21]. Several approaches including metal or nonmetal doping and sensitization with organic and inorganic dyes have been developed to tune the band structure and broaden the light response toward long wave region, and yet more attention should be paid to reduce the binding energy of excitons in the metal oxide, which is of the most importance for promoting the efficiencies of solar energy conversion and PEC water splitting [22–24].

Shaping or tailoring TiO₂ at nanoscale is an avenue to orient charge transport and increase charge transport rate. Controlling chemical growth of 1D nanostructure such as nanorods (NRs), nanofibers (NFs) and nanotubes (NTs) on FTO and ITO conducting glasses offer a “high way” to transport electrons or holes to active sites where water is oxidized to oxygen and protons or protons are reduced to hydrogen [17,25–27]. Compared to the TiO₂ nanoparticle film electrode, the incident photon-to-current conversion efficiency (IPCE) of rutile TiO₂ NRs arrays was greatly increased to ca. 10.0%, which was determined in a

* Corresponding author.

E-mail address: jllong@fzu.edu.cn (J. Long).

¹ Co-first author.

three-electrode system at 0.5 V vs Ag/AgCl [28]. Several strategies including nitrogen doping, hydrogen treating, gold loading, and dye sensitization have been developed to further increase the photo-conversion efficiency. Alternatively, constructing a type II nanoheterostructure is another promising approach to reduce the exciton binding energy because the internal electric field (IEF) formed at interface of semiconductor/TiO₂ nanorods provides a huge driving force to efficiently separate charge carriers. The main objective of the work is to construct the IEF by the heterojunction strategy for enhancing the PEC overall water splitting over 1D TiO₂ nanorods.

Several pivotal points have been considered for rational design of the type II nanoheterostructured photoanodes for the efficient PEC overall water splitting. One is that based on the band alignment fundamental, the used semiconductor should have appropriate conduction and valence band positions, which must be more negative than those of rutile TiO₂ NRs. Another is that the used semiconductor has a well-matched valence band potential with the water oxidation and a low over-potential for the oxygen evolution reaction. Ta₂O_xN_y is able to fulfill the requirements, which has been shown to be an excellent visible light photocatalyst for oxygen evolution in two-step water splitting [29–33], especially the amorphous Ta₂O_xN_y, the out-of-order surface structure and the abundant unsaturated bonds can offer more active sites for the water oxidation reaction. Choi and coworkers recently reported that the amorphous Ta₂O_xN_y is efficient for improving both UV and visible activities of N-doped TiO₂ anatase nanotubes for PEC [34]. They believed that the passivation of N-doped TiO₂ surface trap states resulted in the enhancement for PEC, but more fundamentals were not uncovered, lack of more deep physical analysis about internal electric field and charge transport. In this work, a different design angle will be showed to validate the assumption of electric field-promoted PEC water splitting. Thereby, a facile synthesis protocol, i.e. the combined post-treatment of dropwise addition, high-temperature calcination, and nitridation, was developed to realize the perfect integration of the two semiconductors to form a core-shell nanostructure. The as-prepared TiO₂@Ta₂O_xN_y photoanodes with a visible light response feature give a 10 fold-enhanced IPCE value of 22.6%, which is determined in a two-electrode system under 390 nm light irradiation. The activity results showed that under AM 1.5 G illumination, the photocurrent output of TiO₂@Ta₂O_xN_y photoanodes reached a stable density of 1.32 mA cm⁻² at 1.23 V vs RHE, and which is 12 times and ca. 4.3 times than that of the pristine TiO₂ and TiO₂@Ta₂O₅ counterparts, respectively. Correspondingly, the oxygen evolution rate was improved from 20.3 to 112.7 mmol m⁻² h⁻¹. A solar-to-chemical energy conversion efficiency of ca. 1.49% was achieved at 1.23 V vs RHE.

2. Experimental section

2.1. Reagents and materials

Hydrochloric acid (Sinopharm Chemical Reagent Co., Ltd, HCl), titanium butoxide (Aladdin, ≥99.0%), and tantalum (V) chloride (J&K Scientific Ltd, 99.9%, TaCl₅) all the reagents were A.R. grade and used without further purification. Fluorine-doped tin oxide (FTO) was used as reaction substrate. Deionized water was used for all the experiments.

2.2. Characterization of as-prepared photoelectrodes

Scanning electron-microscopy images of the samples were taken with a Hitachi S-5800 system. HRTEM images were obtained by a JEOL Model JEM 2010 EX instrument at an accelerating voltage of 200 kV. XRD measurements were performed on a Bruker D8 Advance X-ray diffractometer using Cu Kα1 radiation (λ = 1.5406 Å). The accelerating voltage and the applied current were 40 kV and 40 mA, respectively. XPS spectra were determined on a VG ESCALAB 250 XPS system with a monochromatized Al Kα X-ray source (15 kV, 200 W, 500 μm, pass energy = 20 eV). All binding energies were referenced to the C1 s peak

at 284.6 eV of surface adventitious carbon. UV–vis DRS spectra were recorded on a Varian Cary 500 Scan UV–vis-NIR spectrometer with BaSO₄ as the reference. Photoluminescence (PL) spectra were recorded using FL/FS 920 (Edinburgh Instruments) equipped with a 450 W Xe arc lamp as the excitation source and a red sensitive Peltier element cooled Hamamatsu R2658 PMT as the detector. Excited state lifetimes of the charge carriers were measured with the Delta Pro (HORIBA instruments) using a 357 nm laser as the excitation source and employing Time Correlated Single Photon Counting (TCSPC) technique.

Fluorescence lifetime was calculated with equation (Eq. 1).

$$y = ae^{(-\frac{x}{\tau_1})} + be^{(-\frac{x}{\tau_2})} + ce^{(-\frac{x}{\tau_3})} + y_0 \quad (1)$$

2.3. Photoelectrochemical measurements

PEC measurements were measured using the conventional three-electrode electrochemical cell with a working electrode, a platinum foil counter electrode and a saturated Ag/AgCl electrode as reference electrode. The electrode potential was converted to the reversible hydrogen electrode (RHE) potential according to the Nernst equation (Eq. 2).

$$E_{RHE} = E_{Ag/AgCl} + 0.059 pH + E^{\circ}_{Ag/AgCl} \quad (2)$$

Where E_{RHE} is the converted potential versus RHE, $E^{\circ}_{Ag/AgCl} = 0.22$ V at 25°C, and $E_{Ag/AgCl}$ is the measured potential versus the Ag/AgCl reference. The working electrode was the as-prepared samples. In the experiment, the three electrodes were immersed in a N₂-purged 0.1 M KOH aqueous solution (pH = 13) and the working electrode was the illumination of simulated sunlight (100 mW/cm² from 300 W xenon lamp coupled with an AM 1.5 G filter). The intensity of the light was calibrated by the ILT950 instrument. The Current – potential curve and light/dark short circuit photocurrent response was recorded with a CHI660E workstation. The photo-electrochemical impedance spectroscopy (PEIS) and Mott-schottky experiment that was used to evaluate the properties of the photocatalysts under AC polarization was measured on a Potentiostat (ZAHNER). The PEIS measurement was performed under open-circuit voltage in the 0.1 M KOH aqueous solution. Incident photon conversion to electron (IPCE) spectra was measured at 0.2 V in a two-electrode system against a calibrated silicon photodiode using monochromatic light from a xenon lamp (PV Measurements QEX7).

The incident photo-to-current conversion efficiencies (IPCE) at 0.2 V was calculated with Eq. 3

$$IPCE = \eta_{e^{-}/h^{+}} \eta_{transport} \eta_{interface} = \frac{[j_{ph} (mA/cm^2) \times 1239.8 (V \times nm)]}{P_{mono} (mW/cm^2) \times \lambda (nm)} \quad (3)$$

2.4. Hydrogen and oxygen evolution measurements

The photoelectrocatalytic oxygen evolution experiments were performed in a relatively vacuum system allocated an external glass reaction cell by the Labsolar-II photocatalytic water decomposition hydrogen production system (Prefect light company). This typical experiment was measured using the conventional three-electrode electrochemical cell with a working electrode, a platinum foil counter electrode and a saturated Ag/AgCl electrode as reference electrode. The working electrode was the as-prepared samples. In the experiment, the three electrodes were immersed in 0.1 M KOH electrolyte solution (pH = 13) and the temperature of the glass reaction cell was sustained at about 278 K by circulating water. Prior to the reaction procedure, the whole system was slowly evacuated of the air by a vacuum pump until the solution of the glass reaction cell basically kept stable. In order to completely remove the system air, the evacuation was sustained 10 min and finally the blank sample was injected into the gas chromatograph to

define whether the air was completely removed. The working electrode was the illumination of simulated sunlight (100 mW/cm² from 300 W xenon lamp coupled with an AM 1.5 G filter). The evolved oxygen gas was circulated with a micro diffusion pump in this system and its amount was determined by an online gas chromatograph (SHIMADZU GC-8 A, TCD, 5 A, Ar carrier).

The solar-to-chemical energy conversion (SCC) efficiency at 1.23 V vs RHE was calculated with Eq. 4

$$SCC = \frac{[\Delta G \text{ for } H_2 \text{ production (J mol}^{-1})][H_2 \text{ production (mol}^{-1})]}{[\text{total input energy (W)}][\text{reaction time (s)}]} \times 100\% \quad (4)$$

The Gibbs free energy for H₂ generation is 237 kJ mol⁻¹. The overall irradiance of the Xe lamp with AM 1.5 G filter is 100 mW cm⁻², and the irradiation area is 1.0 cm⁻². The irradiance of the Xe lamp was measured by a light intensity meter (ILT950).

3. Results and discussion

3.1. The preparation and structural characterization of TiO₂@Ta₂O₅N_y photoanodes

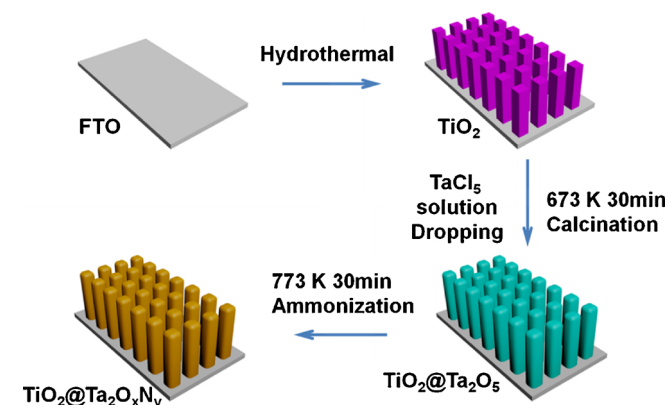
The bare TiO₂ NRs arrays (denoted as TiO₂ below) were grown on FTO substrate by a simple hydrothermal method reported in our previous work [35], and then post-treated by a combining protocol of dropwise addition, high-temperature calcination, and nitridation to prepare the TiO₂@Ta₂O₅N_y NRs arrays, as depicted in Scheme 1. The first step is to form a Ta₂O₅ layer on the surface of TiO₂ NRs. The certain volume amount of TaCl₅ solution (10 mM in ethanol) was dropped on the surface of TiO₂ NRs, rinsed with deionized water and dried in air at room temperature. After the dropwise process was repeated 4–6 times, the as-prepared samples were annealed at 673 K (for 30 min) to produce the Ta₂O₅ layer coated on surface of rutile NRs (denoted as TiO₂@Ta₂O₅). The EDS mapping results (Fig. S1, see supporting materials) clearly show that TiO₂ NRs were enwrapped fully by the Ta₂O₅ layer. The second step is to convert the Ta₂O₅ layer to the Ta₂O₅N_y layer by the post-nitridation at 773 K with an ammonia flow rate of 100 mL/min. The as-synthesized TiO₂@Ta₂O₅N_y electrodes are denoted as TON-x (Where x is the dropped volume amount of TaCl₅ ethanol solution). Finally, three TiO₂@Ta₂O₅N_y photoanodes, TON-60, TON-75 and TON-90, were obtained successfully.

All as-prepared photoanodes were characterized with X-ray powder diffraction (XRD) spectroscopy, in order to determine the crystal structure and possible phase changes, as shown in Fig. 1A. After subtracting the XRD peaks of the FTO glass substrate, all diffraction peaks were indexed to the characteristic peaks of tetragonal rutile TiO₂ (JCPDS No. 88-1175). The most dominant peak centered at 36.5° corresponds to the (101) crystal plane, indicating the growth orientation of

TiO₂. After enwrapping the Ta₂O₅ layer, the intensity of diffraction peaks is slightly decreased, but no diffraction peaks of Ta₂O₅ are observed, suggesting that the Ta₂O₅ layer is in the form of amorphous. After doping nitrogen into Ta₂O₅ at high temperature, there are no any changes in the XRD patterns of the as-prepared TON-x samples, indicating that the post-nitridation does not alter the crystalline phase. Slightly different, the XRD peak located at 43°, belonging to the FTO substrate, is indiscernible, even disappeared for TON-90 and TiO₂@Ta₂O₅. It is possibly because the coverage of Ta₂O₅N_y or Ta₂O₅ and makes the electrode disordered structurally at the direction of 43° angle. Importantly, the nitridation is able to change the optical properties, as displayed in Fig. 2B representing the UV–vis diffuse reflectance spectroscopy (UV–vis DRS) spectra of the as-prepared samples. Obvious, the optical absorption of pure Ta₂O₅N_y powders shows a visible light response. The formation of the Ta₂O₅N_y layer extends the photo-response of TiO₂ to visible light region. The band-gap absorption of TiO₂ shifts from ca. 410 nm to 420 nm (corresponding to the band-gap energy of 2.95 eV) for TON-75, and the shift is further intensified with increasing the thickness of Ta₂O₅N_y layer. The results suggest that the TON-x photoanodes can utilize visible light to split water into hydrogen and oxygen.

Fig. 2 displays the SEM images of bare TiO₂ and TON-75 photoanodes. The low magnification SEM image of the bare TiO₂ photoanode reveals that the conducting surface of the FTO substrate is covered entirely and uniformly with TiO₂ NRs (Fig. 2A). The insert gives a cross-sectional view, showing that these nanorods with a length of about 2.5 μm and an average diameter of ca. 200 nm are nearly perpendicular to the FTO substrate. The side and top facets of the bare TiO₂ NRs are smooth as shown in Fig. 2B. It is slightly different for the TON-75 photoanode, the nanorods of which have the most ambiguous and rough surface (Fig. 2C and D) due to the coating of the amorphous Ta₂O₅N_y layer. The SEM images of TON-60 and TON-90 also show rough surface coatings and the thickness of layers increase with the volume of TaCl₅ solution added (Fig. S2 see supporting materials). The results are further confirmed by the TEM and HRTEM images of the nanorods shown in Fig. 3 and Fig. S3, 4 (see supporting materials). The surfaces of the bare TiO₂ NRs are very clean and smooth (Fig. 3A). It can be clearly seen from Fig. 3B that the typical lattice fringes with the *d* spacings of ca. 0.32 and 0.29 nm are indexed, respectively, to the (110) and (001) crystal planes of rutile TiO₂. However, the surfaces of TON-75 NRs are very rough (Fig. 3C). The HRTEM analysis of the TON-75 NRs displays the overlayer with a ca. 20 nm thickness, which contacts intimately with the TiO₂ core (Fig. 3D). It can appear that there are no obvious lattice fringes for the Ta₂O₅N_y layer, conforming directly that the Ta₂O₅N_y layer is amorphous. The distinct boundary between the TiO₂ and Ta₂O₅N_y layer is a direct evidence for the heterojunction formed between two semiconductors. The EDS mapping results of TON-75 shown in Fig. 3 give four elements, Ti, O, Ta, and N. The N element is evenly distributed on the surface of the TiO₂ NRs, showing that N was doped uniformly into the Ta₂O₅ layer. The TEM images and EDS mapping results of TON-60 and TON-90 (Fig. S3 and 4, see supporting materials) further confirmed that the thickness of Ta₂O₅N_y layers increases with the volume of TaCl₅ solution added into TiO₂ NRs.

To reveal the chemical states of N dopant, XPS was conducted on the TiO₂@Ta₂O₅ and TON-x photoanodes. The full scan spectra survey of TON-75 (Fig. S5, see supporting materials) demonstrates the existence of O, Ti, N, Ta and adventitious C, without other impurity elements. The high-resolution N1 s spectrum shown in Fig. 4A can be resolved into two peaks centered at ca. 404.29 and 399.5 eV, which can be ascribed, respectively, to Ta 4p_{3/2} and N1 s [34]. The binding energy of N species is significantly lower than those of NO (402.7 eV), NO₂ (404.3 eV), and NO₃⁻ (407.3 eV) and yet higher than that of NH₃ (398.7 eV) and metal nitrides (396.0 eV), mostly like that of N species doped in anatase TiO₂ [36]. It indicates that N is homogeneously doped into the lattice oxygen sites of amorphous Ta₂O₅, without the formation of other impurity phases including TaON, Ta₃N₅ and TiN. Surface N



Scheme 1. The schematic diagram of the fabrication procedure of TiO₂@Ta₂O₅N_y NRs arrays.

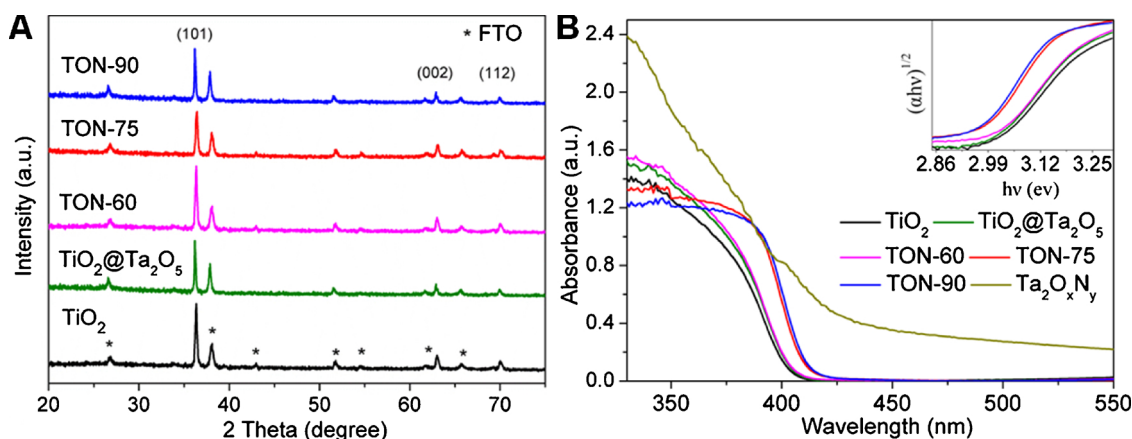


Fig. 1. (A) XRD patterns and (B) UV-Vis absorption spectra of TiO₂, TiO₂@Ta₂O₅, TON-60, TON-75, TON-90 and Ta₂O_xN_y samples.

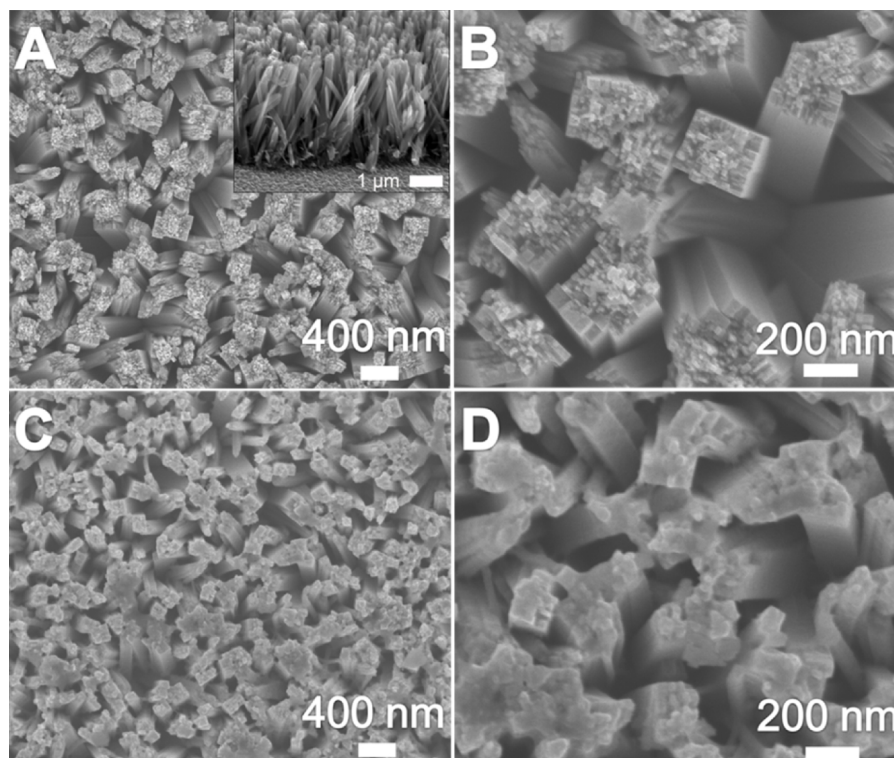


Fig. 2. Top-view SEM images of TiO₂ NRs (A and B) and TON-75 NRs (C and D). The inset to A shows the bare TiO₂ NRs cross-sectional views.

content estimated using photoelectron cross sections calculated by Scofield for three TON-x samples are listed in Table S1 (see supporting materials). The N content is equal to 2.44, 2.72, and 3.18 at.% for TON-60, -75, and -90 samples, respectively. It is highly depended on the thickness of Ta₂O₅ layer, implying that N is indeed doped into the amorphous Ta₂O₅ layer. The substitution of O with N increases the electron density of around Ta atoms, consequently the XPS peaks corresponding to Ta 4f_{7/2} (26.3 eV) and Ta 4f_{5/2} (28.2 eV) are slightly shifted by ca. 0.3 eV to lower binding energy compared to those of Ta₂O₅ (Ta 4f_{7/2} = 26.6 eV and Ta 4f_{5/2} = 28.5 eV) (Fig. 4D). The result agrees well with the values reported in literature [34], further verifying the formation of Ta₂O_xN_y.

3.2. Photoelectrochemical activity for water oxidation

What does the amorphous Ta₂O_xN_y overlayer do for the PEC water splitting? We studied first their photocurrent densities in a three-electrode system equipped with an Ag/AgCl reference electrode and a Pt

foils counter electrode. Fig. 5A shows the linear sweep voltammetry curves of the bare TiO₂, TiO₂@Ta₂O₅, and TON-75 photoanodes. It can appear that the photocurrent densities of TiO₂, TiO₂@Ta₂O₅, and TON-75 are equal, respectively, to 0.11, 0.31, and 1.32 mA/cm² at 1.23 V vs RHE under simulated sunlight irradiation. The photocurrent curve of the TON-75 photoanode rises at around 0.31 V vs RHE and rapidly increases above this potential, reaching up to 1.32 mA/cm² at 1.23 V vs RHE. It is 12 times and 4.3 times than that of the pristine TiO₂ and TiO₂@Ta₂O₅, respectively. In comparison with bare TiO₂, the onset potential of TON-75 is decreased by 100 mV. Moreover, it can be found that there is an optimal thickness of the Ta₂O_xN_y layer. Among three TON-x photoanodes, the TON-75 shows a maximum photocurrent density. More than the thickness of 10 nm, the photocurrent density is decreased significantly (Fig. 5B). For example, TON-90, its photocurrent density is obviously lower than TON-75. This is attributed mainly to two points: (1) A part of UV photons cannot penetrate the overlayer. They may be absorbed by the overlayer, instead of TiO₂; (2) the part of holes photogenerated in TiO₂ is hard to pass through the

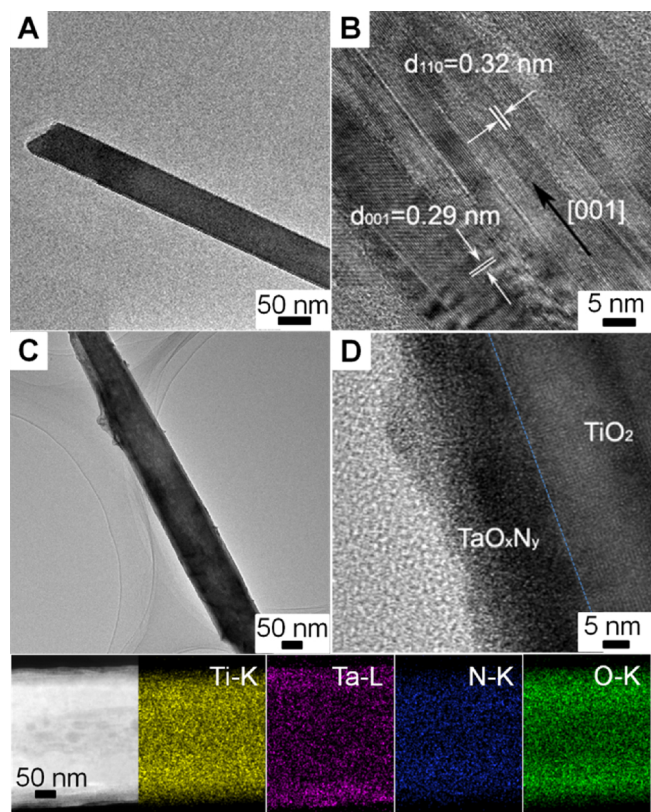


Fig. 3. TEM and HRTEM images of (A) and (B) the TiO_2 nanorod; (C) and (D) the TON-75 nanorod. (E) the mapping images of the TON-75 NRs.

overlay to the interface of catalyst/electrolyte. The transient photocurrents, which are recorded at a fixed potential of 1.1 V vs RHE with light on/off cycle (Fig. 5C), clearly indicate the superior photostability. Upon illumination, the photocurrents of all TON-x photoanodes can rapidly reach a steady state and revert to zero when light turns off. There is almost no decay. Also, the enormous enhancement of photocurrent density can be clearly observed under visible light illumination ($\lambda > 400$ nm), as shown in Fig. 5D. The photocurrent density of TiO_2 is negligible due to no visible light absorption, and yet $\text{TiO}_2@ \text{Ta}_2\text{O}_5$ gives a visible photocurrent density of ca. $25 \mu\text{A}/\text{cm}^2$ at 1.23 V vs RHE. The Ta_2O_5 overlayer increases the photocurrent density to ca. $189 \mu\text{A}/\text{cm}^2$ at 1.23 V vs RHE. The results show that the strategy of designing type II nanostructures is efficient for promoting the PEC overall water splitting. Meanwhile, in order to preclude the possibility that the

enhanced performance origins from N-doped TiO_2 , the linear sweep voltammetry curves of the TiO_2 , N-doped TiO_2 (N- TiO_2) and TON-75 photoelectrodes were shown in Fig. S7 (see supporting materials). The onset potential of N- TiO_2 is lower than bare TiO_2 and TON-75 and the photocurrent density increase sharply up to $0.65 \text{ mA}/\text{cm}^2$ after onset potential. From different curves and lower photocurrent density of N- TiO_2 photoelectrodes, it is further confirmed that the enhanced activity is attributed to the Ta_2O_5 layers.

To explore the origin of the enhanced photoactivity, the IPCEs at various wavelengths of TiO_2 , $\text{TiO}_2@ \text{Ta}_2\text{O}_5$, and TON-75 photoanodes were measured in a two-electrode system at a bias of 0.2 V as shown in Fig. 6A. The IPCE spectra are well matched with the UV-vis absorption spectra shown in Fig. 1B. The maximum IPCE is 22.6% for TON-75, 7.6% for $\text{TiO}_2@ \text{Ta}_2\text{O}_5$, and 2.2% for TiO_2 obtained at 390 nm, which is higher than that of $\text{TiO}_2@ \text{BiVO}_4$ photoanodes (IPCE = 21%, at 1.01 V) [37]. In the visible light region, the TON-75 photoanode give a photon-to-electricity conversion efficiency as high as 4% at 410 nm, corresponding to the PEC water oxidation activity shown in Fig. 5D.

H_2 and O_2 gaseous products were determined by a GC connected with a relatively vacuum system allocated an external glass reaction cell under 1.5 G sunlight irradiation at a bias of 1.23 V vs RHE. It can be seen from Fig. 6B that the evolution of H_2 and O_2 was almost stoichiometric. The evolution rates of H_2 and O_2 is up to $244.2 \text{ mmol m}^{-2} \text{ h}^{-1}$ and $112.7 \text{ mmol m}^{-2} \text{ h}^{-1}$, respectively. The evolution production of H_2 and O_2 is not in stoichiometric value due to the dissolution of O_2 in water [38]. The faradaic efficiencies (η) of oxygen/hydrogen generations on the electrodes were calculated by Eq. 5.

$$\eta = \frac{1}{4} F n Q_{\text{ph}} \quad (5)$$

Where F is the Faraday constant ($96485 \text{ C}/\text{mol}$), n is the mole amount of produced O_2 (H_2), z is the number of transferred electrons per mole of evolved gas (4 for O_2 and 2 for H_2), and Q_{ph} is the integrated photogenerated charge. The faradaic efficiencies of TON-75 were 96.53% and 88% for H_2 and O_2 generations, respectively. The bare TiO_2 photoanode produces the trace amount of H_2 and O_2 under the same conditions. After 5 h of reaction, the gaseous products were determined as shown in Fig. S8 (see supporting materials). The faradaic efficiencies were 92.23% and 80.79% for H_2 and O_2 generation, respectively. It was calculated that the SCC efficiency of the TON-75 electrode for the overall water splitting is equal to ca. 1.49% at 1.23 V vs. RHE, showing a 5-fold enhancement compared to that (0.3%) of bare TiO_2 electrode.

3.3. Proposed mechanism of enhance PEC performance

It was well known that a catalytic reaction commonly involves the adsorption and activation of reactive substrates and the desorption of products. The surface area of TON-75 photoelectrodes is equal to

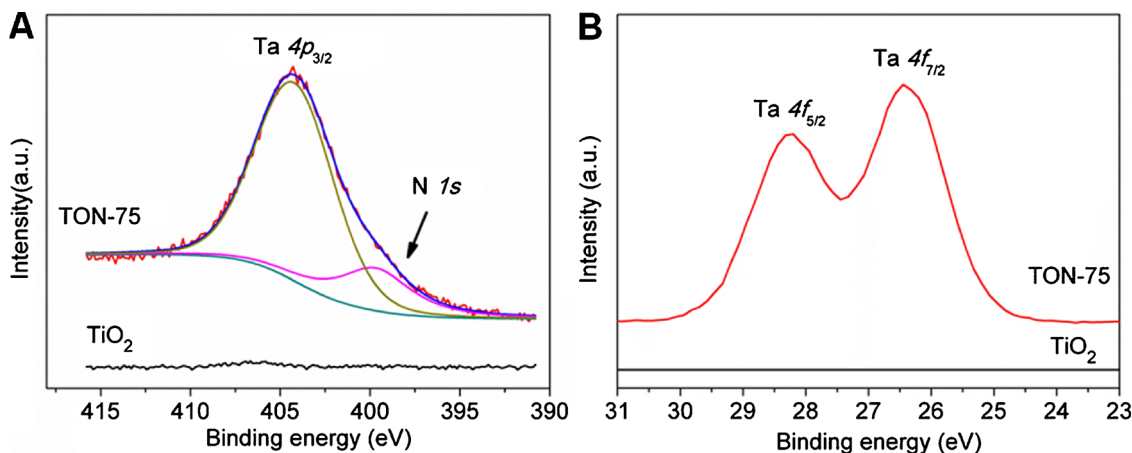


Fig. 4. (A) High-resolution XPS spectra of the N 1s peaks and (B) High-resolution XPS spectra of the Ta 4f peaks of TiO_2 and TON-75 samples.

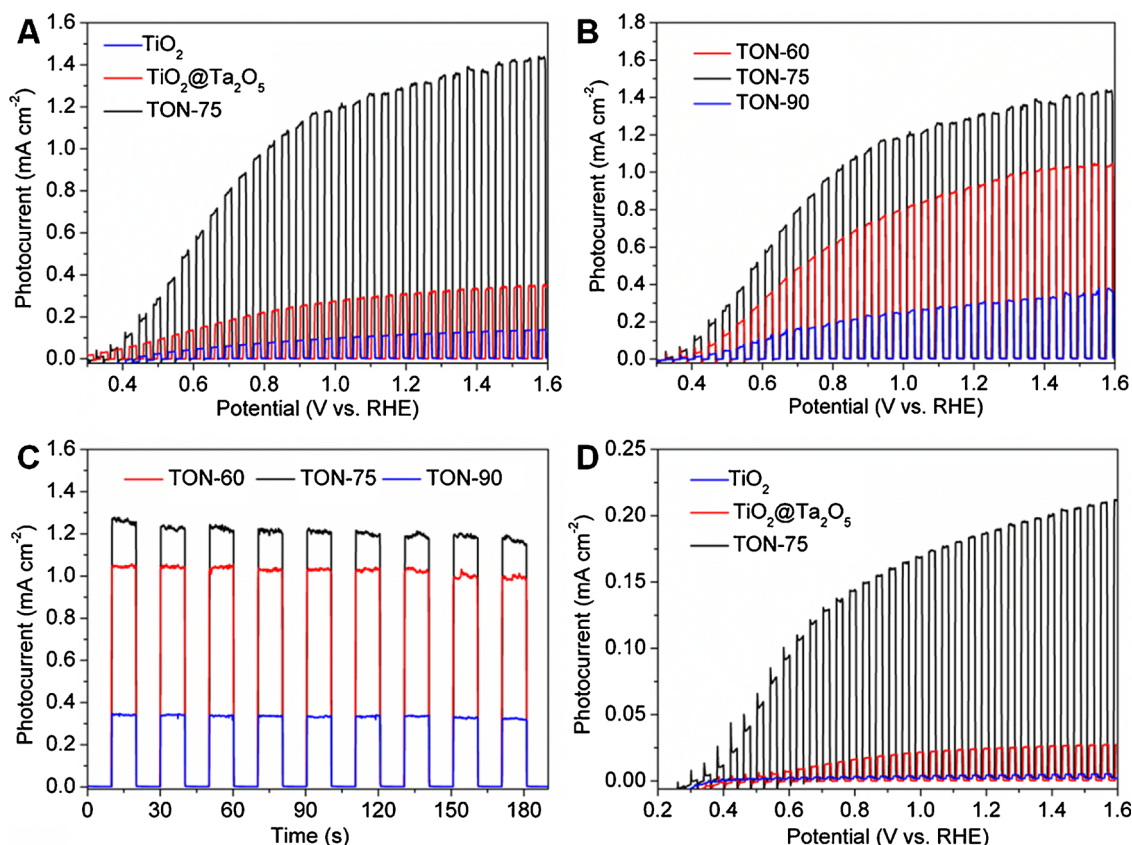


Fig. 5. (A) linear sweep voltammetry curves of TiO_2 , $\text{TiO}_2@\text{Ta}_2\text{O}_5$ and TON-75 photoanodes with intermittent simulated sunlight irradiation. Under the intermittent irradiation simulated sunlight, (B) linear sweep voltammetry curves and (C) transient photocurrents of different $\text{TiO}_2@\text{Ta}_2\text{O}_x\text{N}_y$ photoanodes. (D) linear sweep voltammetry curves of TiO_2 , $\text{TiO}_2@\text{Ta}_2\text{O}_5$ and TON-75 photoanodes with intermittent visible light irradiation ($\lambda > 400 \text{ nm}$).

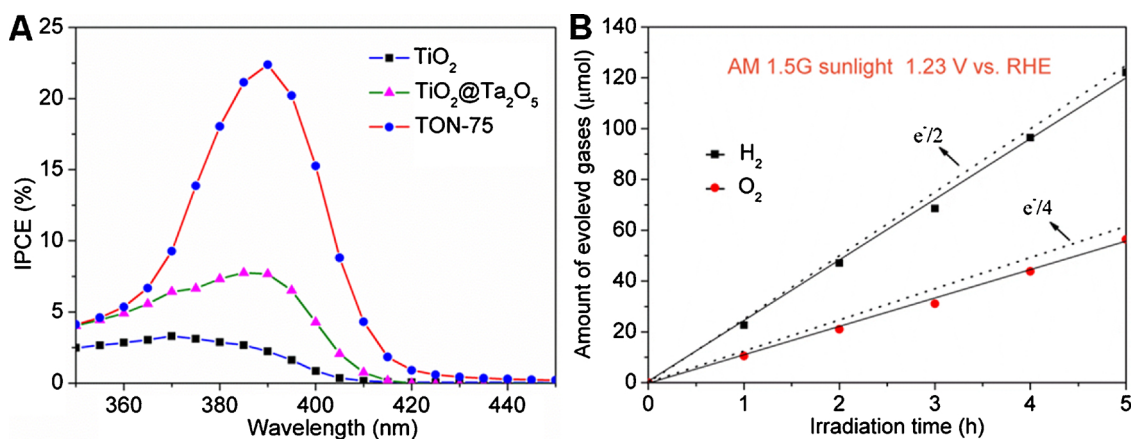


Fig. 6. (A) IPCE patterns of TiO_2 , $\text{TiO}_2@\text{Ta}_2\text{O}_5$ and TON-75 photoanodes and (B) time course of gaseous products during irradiation of the TON-75 photoanode at 1.23 V vs RHE.

$17.61 \text{ cm}^2/\text{g}$ (Fig.S9, see supporting materials). For the PEC overall water splitting reaction, the hydrophilicity-hydrophobicity properties of the electrode surface may be one of the important parameters affecting the water oxidation activity. To reveal clearly the nature of the enhanced PEC water splitting, we firstly examined the interfacial change of TiO_2 NRs before and after coating the $\text{Ta}_2\text{O}_x\text{N}_y$ overlayer by the water contact angle measurement, as displayed in Fig. S10 (see supporting materials). The water contact angle of the bare TiO_2 electrode is 125° , while the TON-75 electrode gives the water contact angle of 121° . The out-of-order surface structure and the abundant unsaturated bonds of the amorphous $\text{Ta}_2\text{O}_x\text{N}_y$ can easily absorb water molecules and offer more active sites for the water oxidation reaction.

As a result, the hydrophilicity property of $\text{TiO}_2@\text{Ta}_2\text{O}_x\text{N}_y$ is much higher than that of TiO_2 . The enhancement in hydrophilicity is positive for the water oxidation, but the overpotential of the electrodes can contribute more to the oxygen evolution reaction (OER) because it determines the rate of oxygen generation on the electrode surface. It can appear from the Fig. 7 that when the Ta_2O_5 layer wraps the TiO_2 NRs surface, the overpotential is significantly increased. After the Ta_2O_5 layer was transformed into the $\text{Ta}_2\text{O}_x\text{N}_y$ layer by the post-nitridation, the overpotential is reduced greatly. The TON-75 electrode shows an oxygen evolution potential of 1.9 V vs. RHE, small than those of $\text{TiO}_2@\text{Ta}_2\text{O}_5$ (2.2 V vs. RHE) and TiO_2 (2.01 V vs. RHE). In other words, the $\text{Ta}_2\text{O}_x\text{N}_y$ overlayer is able to accelerate the oxygen evolution

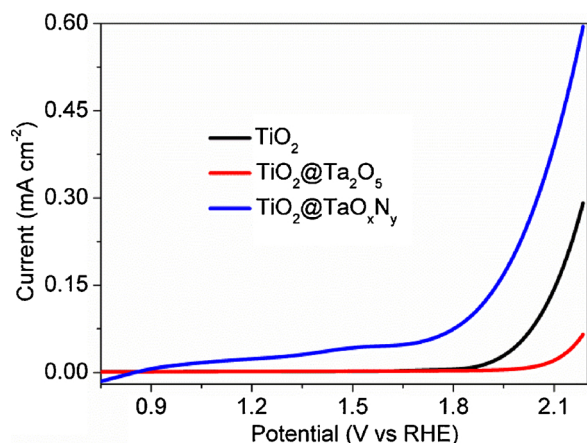


Fig. 7. The overpotential measurements for OER of TiO_2 , $\text{TiO}_2@Ta_2O_5$ and TON-75 photoanodes under the dark reaction conditions.

at the interface of the TON-75 photoanode. Therefore, it can be inferred that the increase in hydrophilicity and the decrease in overpotential of the TON-75 photoanode are main reasons for the enhancement of the faradic efficiencies.

Photoluminescence (PL) spectra (Fig. 8A) of the TiO_2 and TON-75 photoanodes show a broad main emission peak centered at about 430 nm due to the electronic interband transition of rutile TiO_2 . Compared to the TiO_2 photoanode, the PL intensity of the TON-75 photoanode is much weaker, indicating that the direct recombination of electron-holes pairs can be greatly suppressed by the IEF formation in the $\text{TiO}_2@Ta_2O_5$ NRs. To further confirm the conclusion, the fluorescence lifetimes of the TiO_2 and TON-75 photoanodes were

determined from the decay curves of the emission centered at ca. 430 nm, as shown in Fig. 8B. Fitting the curves with an three exponential equation, it was calculated that the average lifetimes are equal to 0.57 and 0.74 ns for TiO_2 and TON-75, respectively. The increase in charge lifetime provides a powerful evidence for the formation of the type II nanoheterostructure between TiO_2 and Ta_2O_5 , where holes can be efficiently transferred from the excited TiO_2 to the Ta_2O_5 overlayer.

From the slopes of the Mott-Schottky plots (Fig. 8C) of TiO_2 and TON-75 photoanodes, it was calculated by using the following Eq. (6) that the carrier densities (N_d) are equal to $2.0 \times 10^{19} \text{ cm}^{-3}$ for TiO_2 and $2.5 \times 10^{19} \text{ cm}^{-3}$ for TON-75, respectively.

$$N_d = \frac{1.41 \times 10^{32} (\text{cm} \times F^{-2} \times V^{-1})}{\epsilon \times A^2 (\text{cm}^4) \times \text{slope} (F^{-2} \times V^{-1})} \quad (6)$$

where ϵ is the rutile TiO_2 dielectric constant ($\epsilon = 86$), and A is the area of electrodes. The carrier density of the depletion layer at the interface of electrode/electrolyte, corresponding to the hole number, is increased by 25% in the TON-75 photoanode. The result is highly consistent with the PL lifetime results above-mentioned. The photo-electrochemical impedance spectroscopies (PEIS) were performed to characterize the intrinsic electronic transport properties of the photoanodes, as shown in Fig. 8D. Only one semicircle is observed and thus can be fitted with the Randles equivalent circuit model (insert of the Fig. 8D). In this model, the element R_s is the resistance relating to charge transport, which contains the resistance of the FTO substrate, the electrolyte and wire connections in the whole circuit. The elements of $R_{ct, \text{bulk}}$ and $C_{ct, \text{bulk}}$ are related to bulk resistance and bulk capacitance of the charge transfer from the semiconductor to the electrolyte. A smaller radius of the semicircle represents a stronger transportation ability of charge carriers, consequently the better PEC performance. TON-75 has a smaller radius than TiO_2 , indicating the stronger charge-transfer ability, in

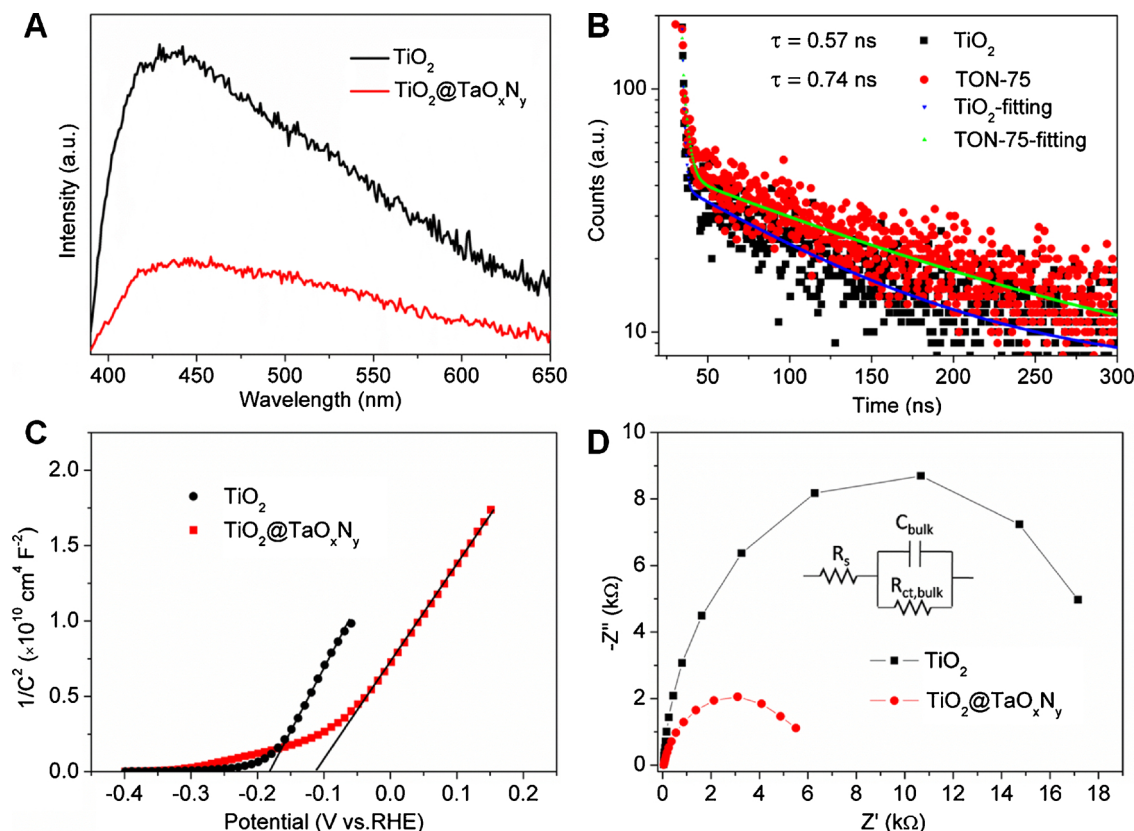
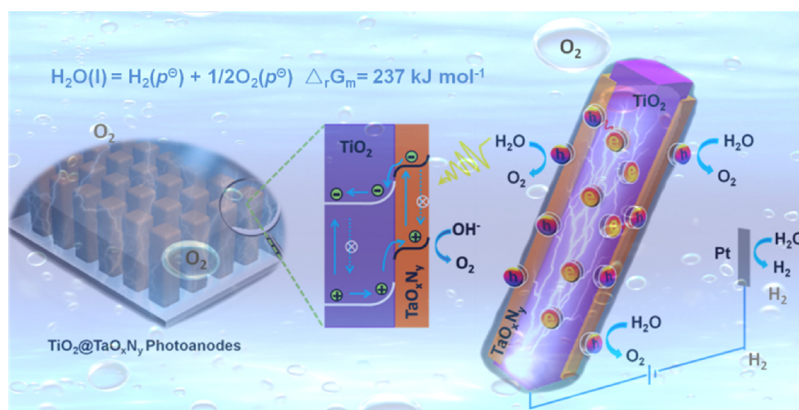


Fig. 8. (A) photoluminescence spectra, (B) photoluminescence decay profiles, (C) Mott-schottky plots, and (D) photo-electrochemical impedance spectra of the photo-excited TiO_2 and TON-75 photoanodes.



Scheme 2. The proposed PEC overall water splitting mechanism in the dual-electrode system.

agreement with the activity results. The curve fitting gives a 13.91 kΩ of bulk resistance ($R_{ct,bulk}$) for rutile TiO_2 NRs and a 2.64 kΩ of bulk resistance for TON-75. The significant decrease in bulk resistance further validates the formation of the inner electric field at the interface of TiO_2 and $Ta_2O_xN_y$ overlayer, which enables the enhancement of carrier separation and transportation.

According to the abovementioned results and analyses, it can be concluded that the type II heterostructure formed between TiO_2 and $Ta_2O_xN_y$ is able to orient the charge flow and to accelerate the hole transport to the active sites for water oxidation. Furthermore, in the viewpoint of the band alignment, the optical band-gap energy of amorphous $Ta_2O_xN_y$ nanoparticles prepared by the same method is ca. 2.86 eV, calculated from the UV–vis DRS spectrum as shown Fig. 1B. The conduction band position of the $Ta_2O_xN_y$ powders is at ca. -0.56 V vs. RHE, determined by Mott-schottky spectrum (Fig. S11, see supporting materials), negative than that (ca. -0.2 eV) of rutile TiO_2 . The valence band position of the $Ta_2O_xN_y$ powders is at +2.3 V vs RHE, also negative than that (ca. +2.8 eV) of rutile TiO_2 [39]. Thus, it is highly reasonable to propose the type II charge-transfer mechanism of the PEC overall water splitting as depicted in Scheme 2. Under the solar light illumination, the $Ta_2O_xN_y$ shell is excited by visible photons, while the core of rutile TiO_2 NRs is excited by UV light to generate electrons and holes. The IEF drives the flow of photogenerated electrons from $Ta_2O_xN_y$ towards TiO_2 with a more positive conduction band energy level, whereas the hole transport is along the opposite direction. Finally, all of photogenerated electrons are transported to the Pt counter electrode to perform the hydrogen evolution reaction, and yet holes are enriched synchronously on the $Ta_2O_xN_y$ outer layer to oxidize water into oxygen gas and produce protons.

4. Conclusions

In summary, the type-II nanostructured $TiO_2@Ta_2O_xN_y$ NRs photoanodes, which were synthesized by a proposed protocol, i.e. the combined post-treatment of dropwise addition, high-temperature calcination, and nitridation, can achieve the 12 fold-enhanced PEC overall water splitting under solar light irradiation and the solar-to-chemical energy conversion efficiency of ca. 1.49% at 1.23 V vs RHE. The characterization results indicated clearly that the IEF formed at the interface of $Ta_2O_xN_y/TiO_2$ orients the charge flow, efficiently separate charge carriers, accelerates the hole transport to water-oxidation sites, resulting in the 10 fold-increased IPCE at 390 nm. This work contributes to a general strategy to design and preparation of efficient photoanodes for solar water splitting.

Acknowledgements

This work was financially supported by the NSFC (Grants No.

21773031), the Natural Science Foundation of Fujian Province of P. R. China (2018J01686), and the State Key Laboratory of Photocatalysis on Energy and Environment (SKLPEE-2017A01 and SKLPEE-2017B02).

Appendix A. Supplementary data

Supplementary material related to this article can be found, in the online version, at doi:<https://doi.org/10.1016/j.apcatb.2018.10.024>.

References

- [1] Y. Sasaki, H. Kato, A. Kudo, *J. Am. Chem. Soc.* 135 (2013) 5441–5449.
- [2] C. Liu, J. Tang, H.M. Chen, B. Liu, P. Yang, *Nano Lett.* 13 (2013) 2989–2992.
- [3] F. Li, K. Fan, B. Xu, E. Gabrielson, Q. Daniel, L. Li, L. Sun, *J. Am. Chem. Soc.* 137 (2015) 9153–9159.
- [4] M. Higashi, K. Domen, R. Abe, *J. Am. Chem. Soc.* 134 (2012) 6968–6971.
- [5] M.H. Ryu Abe, Kazunari Domen, *J. Am. Chem. Soc.* 132 (2010) 11828–11829.
- [6] J. Tian, Y. Sang, G. Yu, H. Jiang, X. Mu, H. Liu, *Adv. Mater.* 25 (2013) 5075–5080.
- [7] J. He, L. Chen, Z.Q. Yi, C.T. Au, S.F. Yin, *Ind. Eng. Chem. Res.* 55 (2016) 8327–8333.
- [8] J. He, L. Chen, F. Wang, Y. Liu, P. Chen, C.T. Au, S.F. Yin, *ChemSusChem* 9 (2016) 624–630.
- [9] J.A.H. Steven, Y. Reece, Kimberly Sung, Thomas D. Jarvi, Arthur J. Esswein, D.G.N. Joep, J.H. Pijpers, *Science* 334 (2011) 645–648.
- [10] D.G. Nocera, *Acc. Chem. Res.* 45 (2011) 767–776.
- [11] B.D. Sherman, M.V. Sheridan, K.R. Wee, S.L. Marquard, D. Wang, L. Alibabaei, D.L. Ashford, T.J. Meyer, *J. Am. Chem. Soc.* 138 (2016) 16745–16753.
- [12] C.A. Mesa, A. Kafizas, L. Francas, S.R. Pendlebury, E. Pastor, Y. Ma, F. Le Formal, M.T. Mayer, M. Gratzel, J.R. Durrant, *J. Am. Chem. Soc.* 139 (2017) 11537–11543.
- [13] S. Hoang, S.P. Berglund, N.T. Hahn, A.J. Bard, C.B. Mullins, *J. Am. Chem. Soc.* 134 (2012) 3659–3662.
- [14] D. Eisenberg, H.S. Ahn, A.J. Bard, *J. Am. Chem. Soc.* 136 (2014) 14011–14014.
- [15] Y.S. Chen, J.S. Manser, P.V. Kamat, *J. Am. Chem. Soc.* 137 (2015) 974–981.
- [16] M. Wang, J. Iocozia, L. Sun, C. Lin, Z. Lin, *Energy Environ. Sci.* 7 (2014) 2182–2202.
- [17] S. Kment, F. Riboni, S. Pausova, L. Wang, L. Wang, H. Han, Z. Hubicka, J. Krysa, P. Schmuki, R. Zboril, *Chem. Soc. Rev.* 46 (2017) 3716–3769.
- [18] J. Long, H. Chang, Q. Gu, J. Xu, L. Fan, S. Wang, Y. Zhou, W. Wei, L. Huang, X. Wang, P. Liu, W. Huang, *Energy Environ. Sci.* 7 (2014) 973.
- [19] B.La.E.S. Aydil, *J. Am. Chem. Soc.* 131 (2009) 3985–3990.
- [20] W. Kang, M.S. Hybertsen, *Phys. Rev. B* 82 (2010) 085203.
- [21] S.K. Jong Hyeok Park, Allen J. Bard, *Nano Lett.* 6 (2006) 24–28.
- [22] Q. Zhang, D.Q. Lima, I. Lee, F. Zaera, M. Chi, Y. Yin, *Angew. Chem. Int. Ed. Engl.* 50 (2011) 7088–7092.
- [23] W. Guo, C. Xu, X. Wang, S. Wang, C. Pan, C. Lin, Z.L. Wang, *J. Am. Chem. Soc.* 134 (2012) 4437–4441.
- [24] A.O. Suil In, Regina Berg, Felipe Garci, S.P.-J. Mintcho, S. Tikhov, A.R.M.L. Dominic, S. Wright, *J. Am. Chem. Soc.* 129 (2007) 13790–13791.
- [25] H.B. Wu, H.H. Hng, X.W. Lou, *Adv. Mater.* 24 (2012) 2567–2571.
- [26] F. Dong, W. Zhao, Z. Wu, *Nanotechnology* 19 (2008) 365607.
- [27] I.S. Cho, Z. Chen, A.J. Forman, D.R. Kim, P.M. Rao, T.F. Jaramillo, X. Zheng, *Nano Lett.* 11 (2011) 4978–4984.
- [28] G. Wang, X. Xiao, W. Li, Z. Lin, Z. Zhao, C. Chen, C. Wang, Y. Li, X. Huang, L. Miao, C. Jiang, Y. Huang, X. Duan, *Nano Lett.* 15 (2015) 4692–4698.
- [29] S. Chen, Y. Qi, T. Hisatomi, Q. Ding, T. Asai, Z. Li, S.S. Ma, F. Zhang, K. Domen, C. Li, *Angew. Chem. Int. Ed. Engl.* 54 (2015) 8498–8501.
- [30] A. Nakada, T. Nakashima, K. Sekizawa, K. Maeda, O. Ishitani, *Chem. Science* 7 (2016) 4364–4371.
- [31] Z. Wang, J. Hou, S. Jiao, K. Huang, H. Zhu, *J. Mater. Chem.* 22 (2012) 21972.

- [32] S.C. Yan, S.B. Lv, Z.S. Li, Z.G. Zou, Dalton Trans. 39 (2010) 1488–1491.
- [33] K. Maeda, R. Abe, K. Domen, J. Phys. Chem. C 115 (2011) 3057–3064.
- [34] H.-i. Kim, D. Monllor-Satoca, W. Kim, W. Choi, Energy Environ. Sci. 8 (2015) 247–257.
- [35] H. Zhuang, J. Miao, H. Huang, J. Long, Y. Zhang, H. Yang, S. He, Y. Yang, X. Wang, B. Liu, ChemPhysChem 16 (2015) 1352–1355.
- [36] Z. Zhang, X. Wang, J. Long, Q. Gu, Z. Ding, X. Fu, J. Catal. 276 (2010) 201–214.
- [37] X. Zhang, B. Zhang, K. Cao, J. Brillet, J. Chen, M. Wang, Y. Shen, J. Mater. Chem. A 3 (2015) 21630–21636S.
- [38] Hara, M. Yoshimizu, S. Tanigawa, L. Ni, B. Ohtani, H. Irie, J. Phys. Chem. C 116 (2012) 17458–17463.
- [39] D.O. Scanlon, C.W. Dunnill, J. Buckeridge, S.A. Shevlin, A.J. Logsdail, S.M. Woodley, C.R. Catlow, M.J. Powell, R.G. Palgrave, I.P. Parkin, G.W. Watson, T.W. Keal, P. Sherwood, A. Walsh, A.A. Sokol, Nat. Mater. 12 (2013) 798–801.